

Anisotropic Field-of-Views in Radial Imaging

Peder E. Z. Larson*, Paul T. Gurney, and Dwight G. Nishimura, *Member, IEEE*

Abstract—Radial imaging techniques, such as projection-reconstruction (PR), are used in magnetic resonance imaging (MRI) for dynamic imaging, angiography, and short- T_2 imaging. They are robust to flow and motion, have diffuse aliasing patterns, and support short readouts and echo times. One drawback is that standard implementations do not support anisotropic field-of-view (FOV) shapes, which are used to match the imaging parameters to the object or region-of-interest. A set of fast, simple algorithms for 2-D and 3-D PR, and 3-D cones acquisitions are introduced that match the sampling density in frequency space to the desired FOV shape. Tailoring the acquisitions allows for reduction of aliasing artifacts in undersampled applications or scan time reductions without introducing aliasing in fully-sampled applications. It also makes possible new radial imaging applications that were previously unsuitable, such as imaging elongated regions or thin slabs. 2-D PR longitudinal leg images and thin-slab, single breath-hold 3-D PR abdomen images, both with isotropic resolution, demonstrate these new possibilities. No scan time to volume efficiency is lost by using anisotropic FOVs. The acquisition trajectories can be computed on a scan by scan basis.

Index Terms—Anisotropic field-of-view (FOV), projection-reconstruction (PR), radial imaging, three-dimensional (3-D) cones.

I. INTRODUCTION

RADIAL medical imaging methods were first used in X-ray computerized tomography (CT) where data is acquired on radial projections. These projections correspond to radial lines in frequency space, a fact that inspired the first magnetic resonance imaging (MRI) acquisitions to also occur on radial lines [1]. These 2-D imaging methods are also known as projection-reconstruction (PR) and projection acquisition (PA). Radial imaging also refers to the 3-D acquisition techniques of 3-D PR and 3-D cones [2], [3].

Radial MRI is used for dynamic imaging applications because it is inherently robust to motion [4] and flow [5]. It is used in angiography [6], with applications such as contrast-enhanced angiography [7], [8] and time-resolved angiography [9]. Radial MRI readouts can support very short repetition times (TRs) and echo times (TEs). Short TRs are useful for steady-state free precession (SSFP) imaging, particularly if high resolution is required or for quadrature fat/water separation. Both the short TRs and robustness to motion and flow have been taken advantage of in balanced SSFP coronary artery imaging [10], [11]. Short TEs are required for ultra-short echo time (UTE) MRI, which

Manuscript received October 2, 2006; revised June 4, 2007. This work was supported in part by the National Institutes of Health under Grants 2R01-HL39297 and Grant 1R01-EB002524, and in part by GE Medical Systems. Asterisk indicates corresponding author.

*P. E. Z. Larson is with the Magnetic Resonance Systems Research Laboratory, Stanford University, Stanford, CA 94305 USA (e-mail: peder@mrsrl.stanford.edu).

P. T. Gurney and D. G. Nishimura are with the Magnetic Resonance Systems Research Laboratory, Stanford University, Stanford, CA 94305 USA.

Digital Object Identifier 10.1109/TMI.2007.902799

can image collagen-rich tissues such as tendons, ligaments and menisci, as well as calcifications, myelin, periosteum, and cortical bone [12], [13]. In addition to 2-D acquisitions, 3-D radial imaging techniques, such as 3-D PR [14] and 3-D cones [15], have been applied to UTE.

Three-dimensional PR is used for the vastly undersampled isotropic projection reconstruction (VIPR) imaging method [7] for MR angiography and efficient phase-contrast flow imaging [16]. The isotropic resolution of 3-D PR is advantageous for multiplanar and 3-D reformats. VIPR uses undersampled acquisitions because the number of projections required for fully-sampled 3-D PR is prohibitively large. The undersampling is tolerated because of the diffuse aliasing properties of radial trajectories [7]. Another solution to the often prohibitively large number of projections required by 3-D PR is to use conical trajectories [2], [3]. These sample in a spiral pattern along cones with various projection angles, allowing for significantly faster volumetric coverage than 3-D PR.

In 2-D and 3-D PR trajectories, as well as 3-D cones, a critical number of projection angles must be acquired to support a given field-of-view (FOV)—also referred to as a region-of-support or region-of-interest. The lines are normally acquired with equiangular spacing, resulting in only circular and spherical FOV shapes. Many imaging applications, however, have anisotropic dimensions and would benefit from anisotropic FOVs.

In this paper, we introduce a new method to simply and easily design radial imaging trajectories for anisotropic FOVs. One previous method applied several varying angular density functions to obtain anisotropic 2-D FOVs [17], [18]. Our method also utilizes nonuniform angular spacing, and is able to exactly match the sampling to the desired FOV shape. Design algorithms for 2-D and 3-D PR, as well as 3-D cones are presented. Tailoring the FOV for noncircular objects or regions-of-interest allows for scan time reductions without introducing aliasing artifacts. In undersampled applications, this tailoring will reduce the occurrence of aliasing artifacts. Additionally, our algorithms support anisotropic projection lengths, and, equivalently anisotropic, resolution. This is useful for reducing gradient slew rate demands in 3-D cones, and could also be used for reducing gradient distortion artifacts by favoring the more homogeneous or powerful axes. It can also be used to trade image resolution in certain dimensions for acquisition time.

II. THEORY

In radial imaging, the raw data is acquired on radial lines in frequency space, referred to as “ k -space” in MRI. A discrete number of these lines, also known as projections or spokes, are sampled during data acquisition. Sampling theory tells us that the sample separation determines the FOV. Cartesian samples are generally equally spaced, and the FOV is equal to the inverse

of the sample spacing, $1/\Delta k$. In radial imaging, the spacing between adjacent projections in k -space varies radially, and is most sparse at the end of the projections. The sample spacing along the projections must also be considered, although in MRI this usually does not limit the FOV as much as the distance between projections. We will investigate how this projection separation determines the FOV and resolution. Further discussion of radial sampling theory can be found in [19].

A. FOV Versus PSF

The FOV of a given sampling pattern is characterized by its Fourier transform (\mathcal{FT}), known as the point spread function (PSF). Since the sampling pattern is multiplied by the frequency data, the PSF is convolved with the image data. The central lobe of the PSF introduces a blurring, and thus determines the resolution of the resulting image. Aliasing lobes in the PSF are outside this central lobe and determine the FOV of the resulting image. In radial imaging, the distinct shape of the aliasing lobe determines the FOV, but they are not always the same shape. Convexity of the aliasing lobe shape in the PSF will ensure that the FOV shape is exactly the same. Polygons, rectangles, cuboids, ellipsoids, and ovals are some examples of convex shapes useful for medical imaging. While there are concave PSF shapes that will support concave FOVs, such as a “plus”-sign shape, we will assume convexity since this includes most objects and regions-of-interest in medical imaging.

B. 2-D Sampling

The FOV of a 2-D radial imaging trajectory can be analyzed by decomposition into adjacent spokes. A pair of adjacent spokes can be approximated as two parallel lines, shown in Fig. 1(a) and described mathematically as

$$P(k_x, k_y) = \left[\delta\left(k_y - \frac{\Delta k_\phi}{2}\right) + \delta\left(k_y + \frac{\Delta k_\phi}{2}\right) \right] \text{rect}\left(\frac{k_x}{2k_{\max}}\right) \quad (1)$$

where Δk_ϕ is the separation at the end of the projections and k_{\max} is the extent of the projections. The PSF of (1), illustrated in Fig. 1(b), is

$$\mathcal{FT}\{P(k_x, k_y)\} = C \cos(\pi \Delta k_\phi y) \cdot \text{sinc}(2k_{\max}x) \quad (2)$$

where C includes all scaling factors. The peaks of $|\cos(\pi \Delta k_\phi y)|$ will introduce aliasing when convolved with the object, thus limiting the FOV perpendicularly to the direction of the lines to $1/\Delta k_\phi$. The actual PSF is much more peaked than a cosine because the sample spacings in k_y from other projections introduce phase variations that cause the aliasing to cancel out along y between 0 and $\pm(1/\Delta k_\phi)$, as is shown in the Section IV. This is analogous to Cartesian sampling where the PSF of two parallel lines is also a cosine but phase variations from the other sampling lines cause sharp aliasing peaks. The resolution is limited to a minimum of $1/2k_{\max}$ due the $\text{sinc}(2k_{\max}x)$ term.

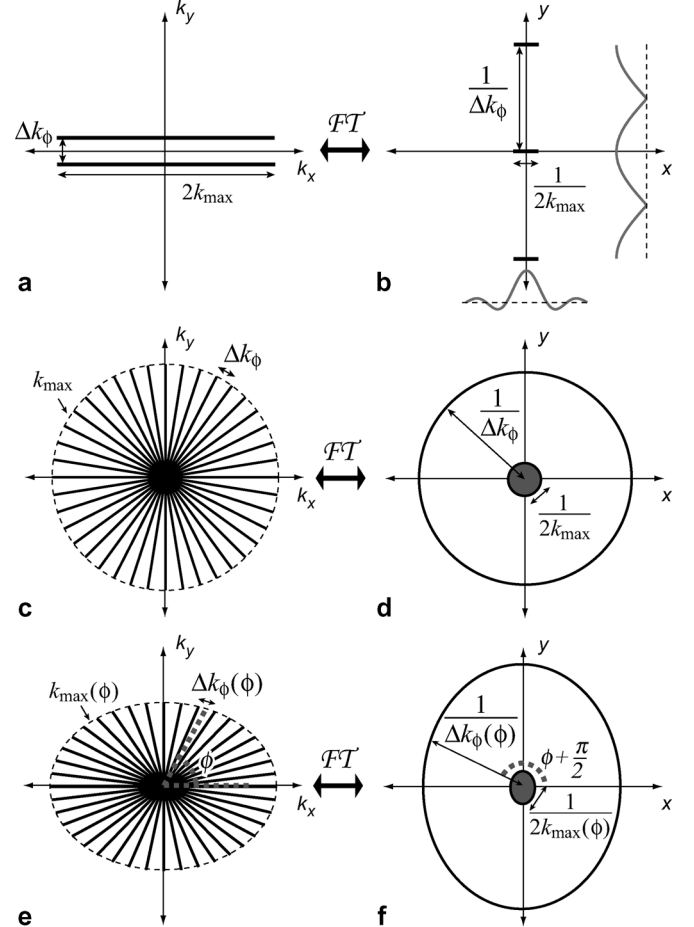


Fig. 1. Sampling in 2-D radial imaging. (a) Approximation of adjacent projections by parallel sampled lines. (b) Parallel lines PSF illustration. The gray lines show the spatial variation derived in (2). Aliasing lobes appear at $1/\Delta k_\phi$. (c) Isotropic PR trajectory with constant angular spacing and extent. (d) Isotropic PR PSF illustration. (e) PR trajectory with variable angular spacing and extent. (f) Angularly varying PR PSF illustration.

If all projections are equally spaced, as shown in Fig. 1(c), the alias-free FOV and resolution, res, are

$$\text{FOV} = \frac{1}{\Delta k_\phi} \approx \frac{1}{k_{\max} \Delta \Theta} = \frac{N}{\pi k_{\max}} \quad (3)$$

$$\text{res} = \frac{1}{2k_{\max}} \quad (4)$$

where $\Delta \Theta$ is the angular spacing between spokes in radians and N is the number of full projections acquired k_{\max} [Fig. 1(d)]. Here, we have used the approximation that $\sin(\Delta \Theta) \approx \Delta \Theta$ for small $\Delta \Theta$.

From Fourier theory, rotation of the parallel lines rotates their \mathcal{FT} , thus the angular spacing between spokes can be varied to produce anisotropic FOV shapes. Similarly, if k_{\max} is varied, the resolution size changes angularly. Equation (2) tells us that the sample spacing at angle ϕ determines the perpendicular FOV, while $k_{\max}(\phi)$ determines the resolution at ϕ . This is shown in Fig. 1(e) and (f), and is formally expressed as

$$\text{FOV}\left(\phi + \frac{\pi}{2}\right) = \frac{1}{\Delta k_\phi(\phi)} \approx \frac{1}{k_{\max}(\phi) \Delta \Theta(\phi)} \quad (5)$$

$$\text{res}(\phi) = \frac{1}{2k_{\max}(\phi)}. \quad (6)$$

Discrete sampling along the parallel lines results in repetition of the \mathcal{FT} pattern (2) in this sampling direction [x in (2) and Fig. 1(a)]. Radial sample spacing of Δk_r results in repetitions at $1/\Delta k_r$. These aliasing lobes are often eliminated in MRI because of low-pass filters applied during the readout. These filters will, however, limit the FOV in the projection direction to $1/\Delta k_r$ because they are matched to the sample spacing. Therefore, the maximum radial sampling spacing must be

$$\Delta k_r \leq \frac{1}{\max(\text{FOV}(\phi))} \quad (7)$$

to ensure there is no aliasing or FOV restrictions due to the sampling along the projections.

C. 3-D Sampling

Radial sampling in 3-D can be analyzed with the same principles as in 2-D. Again, approximating adjacent spokes as a set of parallel lines, we now have

$$P(k_x, k_y, k_z) = \left[\delta\left(k_y - \frac{\Delta k_\phi}{2}\right) + \delta\left(k_y + \frac{\Delta k_\phi}{2}\right) \right] \text{rect}\left(\frac{k_x}{2k_{\max}}\right) \cdot \delta(k_z). \quad (8)$$

The PSF is then the same as (2)

$$\mathcal{FT}\{P(k_x, k_y, k_z)\} = K \cos(\pi \Delta k_\phi y) \cdot \text{sinc}(2k_{\max}x). \quad (9)$$

This aliasing pattern is the same as illustrated in Fig. 1(b), but with an infinite extent in z .

A set of adjacent cones can be modeled by rotating a pair of parallel lines about the k_z axis, as shown in Fig. 2(a), which rotates the PSF of these parallel lines about the z axis. The resulting PSF pattern is circularly symmetric about the z axis and the aliasing lobe has a polar deflection of $\theta + (\pi/2)$ for a cone deflection of θ , shown in Fig. 2(b). We are using a spherical coordinate notation where θ , the polar angle, is the deflection from the positive z axis and ϕ , the azimuthal angle, is the rotation from the positive x axis.

Adjacent projections on a cone produce aliasing patterns that are rotations of the PSF in (9), as illustrated in Fig. 2(c) and (d). The aliasing lobes are the nearest to the origin in the $x - y$ plane at an azimuthal angle $\phi + (\pi/2)$ and at a distance of $1/\Delta k_\phi$. They extend in a direction that is determined by the cone deflection angle, as shown in Fig. 2(d).

Combining these results, we find that the sampling along a cone limits the FOV azimuthally in the $x - y$ plane while the sampling of different cones limits the FOV in the polar direction

$$\text{FOV}_\theta\left(\theta + \frac{\pi}{2}, \phi\right) = \frac{1}{\Delta k_\theta(\theta)} \quad (10)$$

$$\text{FOV}_\phi\left(\theta = \frac{\pi}{2}, \phi + \frac{\pi}{2}\right) = \frac{1}{\Delta k_\phi(\phi)} \quad (11)$$

$$\text{res}(\theta, \phi) = \frac{1}{2k_{\max}(\theta, \phi)} \quad (12)$$

where the variables are all illustrated in Fig. 2. The resolution is determined by the projection extents. The samples along each projection must again satisfy (7).

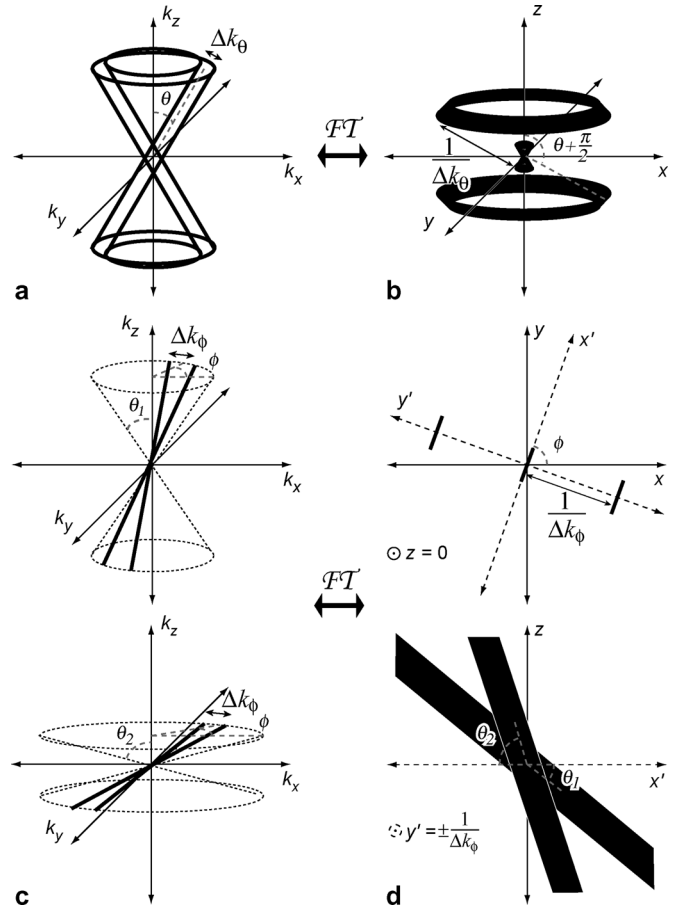


Fig. 2. Sampling in 3-D radial imaging. (a) Approximation of adjacent cones by rotated parallel lines. (b) PSF illustration of adjacent cones model, which is the parallel lines PSF [Fig. 1(b)] rotated around the z axis. (c) Adjacent projections on two different cones. (d) PSF illustrations for the adjacent projections. Top illustration shows the intersection of the PSF with the $x - y$ plane, which is approximately identical for the projections on both cones. Bottom illustration shows the planes which contain the aliasing lobes. These planes are perpendicular to the y' axis at $y' = \pm 1/\Delta k_\phi$, and the lobes extend at different angles depending on the cone angle.

III. METHODS

A. Two-Dimensional Projection-Reconstruction

Two-dimensional radial imaging trajectories can be defined by the projection angles, projection lengths, and the sampling pattern along the projections. Our algorithm designs a set of projection angles, $\Theta[n]$, and projection lengths, $K_{\max}[n]$, for a desired FOV pattern. The sampling pattern along the projections is not designed, and should be chosen to meet the condition in (7).

The algorithm is shown in Fig. 3. The desired FOV must be specified as a function of angle, $\text{FOV}(\phi)$, and must be π -periodic ($\text{FOV}(\phi) = \text{FOV}(\phi + \pi)$). The desired projection lengths can be specified as $k_{\max}(\phi)$, and also must be π -periodic. An initial angle of ϕ_0 may be specified, although the default of $\phi_0 = 0$ is appropriate for most applications. The angular width of the resulting angles, ϕ_{width} , may also be specified, and will be π for most applications, including full-projection PR. One application of varying this width is half-projection PR, where

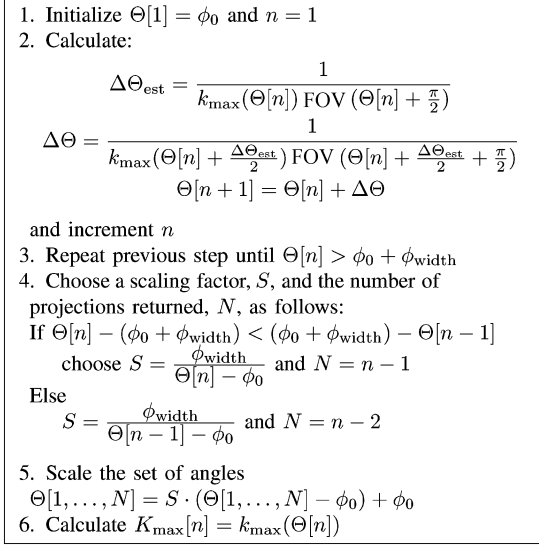


Fig. 3. Generalized 2-D anisotropic FOV radial imaging algorithm.

$\phi_{\text{width}} = 2\pi$ could be used. These parameters are also useful for designing 3-D PR trajectories—see Section III-C.

After initialization, the relationship derived in (5) is used to sequentially calculate a set of projection angles in step 2 of the algorithm. The projection separation is first estimated, $\Delta\Theta_{\text{est}}$, and then the actual projection separation is then calculated using the angle $\Theta[n] + (\Delta\Theta_{\text{est}}/2)$. Without this estimation, the resulting FOV will be very slightly rotated and distorted because the projection separation is centered between $\Theta[n]$ and $\Theta[n+1]$. Since $\Theta[n+1]$ is unknown, $\Theta[n] + (\Delta\Theta_{\text{est}}/2)$ provides a good estimate of the middle angle, especially compared to using $\Theta[n]$. Additional iterations for increased accuracy are possible but provide little additional benefit.

The sequential nature of the algorithm and the required periodicity of the projection angles results in an undesired angle spacing at the end of the design. Steps 4 and 5 correct for this by scaling the set of projection angles to the chosen ϕ_{width} . The scaling slightly distorts the resulting FOV shape so the scaling factor, S , is chosen by step 4 to be as close to 1 as possible. This step could also be modified to require that the number of projections be even, odd, or a scalar multiple for acquisition strategies such as multiecho PR [8].

The computation cost of this algorithm is small since it involves simple calculations and requires no iterations or large matrix operations.

B. Three-Dimensional Cones

The 2-D design algorithm can directly be applied to designing 3-D cones imaging trajectories. The 3-D FOV shapes that are achievable are circularly symmetric about one axis, which we define to be the z axis, corresponding to cones wrapping around the k_z axis as shown in Fig. 2(a) and (b). These shapes can be described by $\text{FOV}(\theta, \phi) = \text{FOV}_\theta(\theta)$, as is illustrated in Fig. 4(a) and (b). For example, a rectangular-shaped $\text{FOV}_\theta(\theta)$ will yield a cylindrical FOV, while an elliptical $\text{FOV}_\theta(\theta)$ yields an ellipsoid.

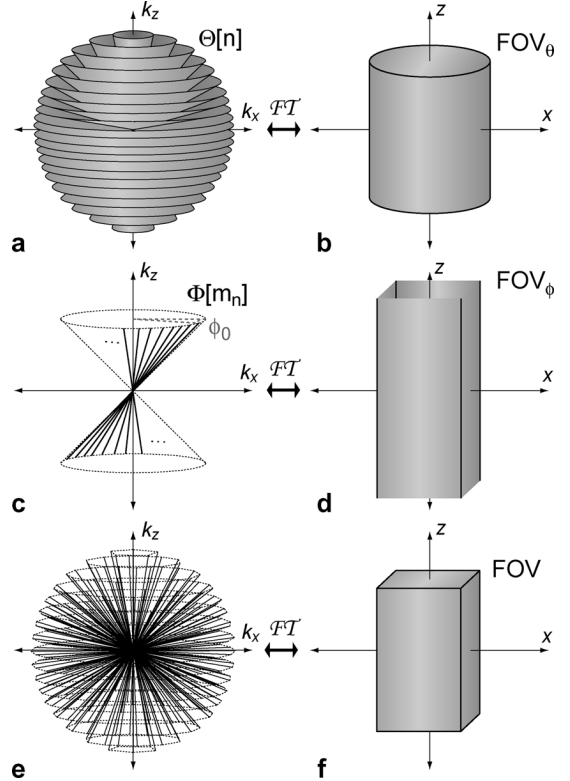


Fig. 4. Three-dimensional radial trajectory design (cones-based). (a) Cones designed with 2-D algorithm. (b) Sampling of cones introduces FOV_θ , which is circularly symmetric about the z axis. (c) Projections on each cone designed with 2-D algorithm using a random starting angle ϕ_0 . (d) Sampling along cones introduces FOV_ϕ , which is approximately independent of z . (e) Three-dimensional PR trajectory resulting from sampling in (a) and (c). (f) Three-dimensional PR FOV is the minimum of FOV_θ (b) and FOV_ϕ (d).

For anisotropic 3-D cones design, the 2-D PR algorithm is used with inputs of $\text{FOV}_\theta(\theta)$ and $k_{\max}(\theta)$ (optional), $\phi_{\text{width}} = \pi$, and $\phi_0 = (2k_{\max})^{-1}(0)\text{FOV}(\pi/2)$. This ϕ_0 ensures that no cones are just a single projection. The resulting set of projection angles and extents describe the set of cones to be used, where the angles, $\Theta[n]$, represent the deflection from the k_z axis. Sampling within each cone and generation of appropriate gradient waveforms are described in [3].

C. Three-Dimensional Projection-Reconstruction

We have created two methods for designing 3-D PR trajectories with anisotropic FOVs. One samples a set of cones, the “cones-based” method, while the other designs and samples a spiraling path, the “spiral-based” method. Fig. 5 shows two resulting sampling patterns for both the cones-based and spiral-based design methods.

1) *Cones-Based Design:* This method designs 3-D projections for an anisotropic FOV by first designing a set of cones and then appropriately sampling on each cone. Isotropic sampling in these two dimensions will result in a spherical FOV, with the number of projections per cone proportional to $\sin(\theta)$ [20], where θ is the polar angle of the cone.

Equations (10) and (11), illustrated in Fig. 2, tell us that the cones sampled will define a limiting FOV that is circularly symmetric about the z axis, $\text{FOV}_\theta(\theta, \phi) = \text{FOV}_\theta(\theta)$, while

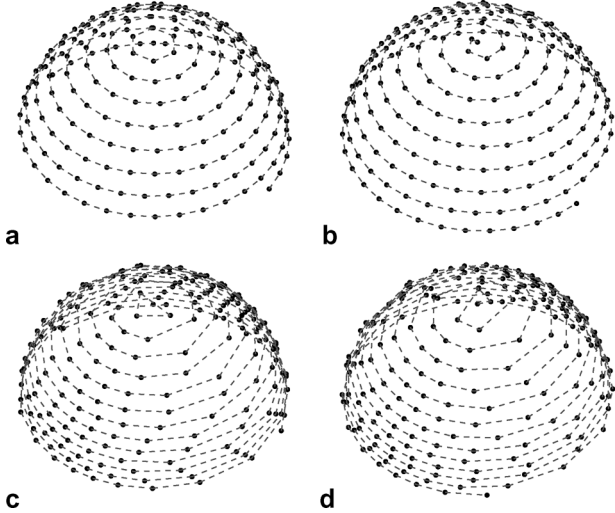


Fig. 5. Three-dimensional PR trajectories. (a) Cones-based design and (b) spiral-based design for uniform sampling, resulting in a spherical FOV. (c) Cones-based design and (d) spiral-based design of an ellipsoid FOV with nonuniform sampling in both the azimuthal and polar directions.

the samples on each cone define a maximum FOV that is approximately invariant in z , $\text{FOV}_\phi(\theta, \phi) \approx \text{FOV}_\phi(x, y)$ [Fig. 4(a)–(d)]. We will describe FOV_ϕ using the deflection angle in cylindrical coordinates, $\phi_c = \tan^{-1}(y/x)$, resulting in the simple notation $\text{FOV}_\phi(x, y) = \text{FOV}_\phi(\phi_c)$. Both sampling patterns limit the FOV, resulting in

$$\text{FOV} = \min(\text{FOV}_\theta(\theta), \text{FOV}_\phi(\phi_c)) \quad (13)$$

as illustrated in Fig. 4(e) and (f).

This method takes inputs of FOV_θ and FOV_ϕ , with

$$\text{FOV}_\phi(\phi_c) \leq \text{FOV}_\theta\left(\frac{\pi}{2}\right) \quad (14)$$

to ensure that the cone spacing does not introduce aliasing inside FOV_ϕ in the $x - y$ plane. $k_{\max,\theta}(\theta)$ can also be used. Varying $k_{\max,\phi}$ has not been incorporated into our algorithm because it causes the polar angle spacing to vary azimuthally, resulting in distortion of the FOV. The cones are designed using the 2-D PR algorithm with $\text{FOV}_\theta(\theta)$, $k_{\max,\theta}(\theta)$, $\theta_0 = 0$, and $\theta_{\text{width}} = \pi/2$. The resulting $\Theta[n]$ and $K_{\max}[n]$, where $n = 1, \dots, N_{\text{cones}}$, are then sampled, also using the 2-D PR design algorithm.

The spokes covering each cone are designed with $\text{FOV}_\phi(\phi_c)$ and $\phi_{\text{width}} = 2\pi$. For cone n , $k_{\max,\phi} = K_{\max}[n] \cdot \sin(\Theta[n])$ to adjust for the variable circumference. The initial angle ϕ_0 on each cone is chosen at random uniformly in the interval $[0, (K_{\max}[n] \cdot \sin(\Theta[n]) \cdot \text{FOV}_\phi(\pi/2))^{-1}]$. This randomization reduces coherent aliasing artifacts that are introduced when $\phi_0 = 0$ for each cone (see Fig. 10). Note that the first cone ($n = 1$) is just a single projection along the k_z axis. The final result is a set of $\Phi[m_n]$ for $m_n = 1, \dots, M_n$ and $n = 1, \dots, N_{\text{cones}}$, where M_n is the number of projections within cone n .

To complete the full-projection design, an additional cone is added in the $k_x - k_y$ plane ($\theta = \pi/2$) that is only azimuthally sampled along half of the circumference. The 2-D PR design algorithm is used, with $\text{FOV}_\phi(\phi_c)$, $k_{\max,\phi} = k_{\max,\theta}(\pi/2)$, a

randomized ϕ_0 , and $\phi_{\text{width}} = \pi$. For half-projection designs, the additional half-sampled cone is not needed and $\theta_{\text{width}} = \pi$ is used for the cone design.

2) *Spiral-Based Design:* This method of 3-D PR design is inspired by a method that isotropically samples the unit sphere on a spiral path [21]. It is similar to the cones-based method, taking the same inputs of FOV_θ and FOV_ϕ , with $\text{FOV}_\theta(\pi/2) = \max(\text{FOV}_\phi(\phi_c))$, and, optionally, $k_{\max,\theta}$. This method is best suited for half-projections, and an extension to full-projection design is described in Appendix I. It also results in a more diffuse aliasing pattern (see Fig. 10).

First, a set of polar sampling angles is designed with the 2-D PR algorithm exactly as in the cones-based method for half-projections, with FOV_θ , $k_{\max,\theta}$, $\theta_0 = 0$, and $\theta_{\text{width}} = \pi$, yielding $\hat{\Theta}[n]$ and $\hat{K}_{\max}[n]$ for $n = 1, \dots, N_{\text{polar}}$. To create a continuous sample path in the longitudinal direction, these sets are linearly interpolated to final samples of $\hat{\Theta}[N_{\text{polar}} + 1] = \pi$ and $\hat{K}_{\max}[N_{\text{polar}} + 1] = k_{\max,\theta}(\pi)$.

The interpolation uses the number of projections required, which is found by estimation using the required number of azimuthal samples on a cone at $\theta = \pi/2$, $N_{\phi,\text{est}}$, as well as $\hat{\Theta}[n]$ and $\hat{K}_{\max}[n]$. The 2-D PR algorithm with FOV_ϕ , $k_{\max,\phi} = k_{\max,\theta}(\pi/2)$, $\phi_0 = 0$, and $\phi_{\text{width}} = 2\pi$ is used to compute $N_{\phi,\text{est}}$. The number of projections between $\hat{\Theta}[n]$ and $\hat{\Theta}[n + 1]$ will be approximately

$$N_{n,\text{est}} = N_{\phi,\text{est}} \sin\left(\frac{\hat{\Theta}[n] + \hat{\Theta}[n + 1]}{2}\right) \times \frac{\hat{K}_{\max}[n] + \hat{K}_{\max}[n + 1]}{2k_{\max,\phi}}. \quad (15)$$

The total number of projections is chosen to be

$$N = \sum_{n=1}^{N_{\text{polar}}} N_{n,\text{est}}. \quad (16)$$

The linear interpolation is done such that there are $N_{n,\text{est}}$ projections between $\hat{\Theta}[n]$ and $\hat{\Theta}[n + 1]$. This is done by using a parametrization, $\theta(t)$, where $\theta(t_n) = \hat{\Theta}[n]$, $t_{n+1} - t_n = N_{n,\text{est}}$, and $t_1 = 1$. The polar projection angles are computed by sampling the linear interpolation of this parametrization as $\Theta[m] = \theta(m)$ for $m = 1, \dots, N$. If variable extents are used, the interpolation of $k(t)$, where $k(t_n) = \hat{K}_{\max}[n]$, is sampled as $K_{\max}[m] = k(m)$.

The azimuthal sampling, $\Phi[m]$, is then computed similarly to step 2 in Fig. 3, with an additional scaling factor also used in the cones-based design to compensate the cone circumference

$$\Delta\Phi_{\text{est}} = \frac{1}{K_{\max}[m] \sin(\Theta[m]) \text{FOV}_\phi(\Phi[m] + \frac{\pi}{2})} \quad (17)$$

$$\Delta\Phi = \frac{1}{K_{\max}[m] \sin(\Theta[m]) \text{FOV}_\phi(\Phi[m] + \frac{\Delta\Phi_{\text{est}}}{2} + \frac{\pi}{2})} \quad (18)$$

$$\Phi[m + 1] = \Phi[m] + \Delta\Phi \quad (19)$$

with the initial angle of $\Phi[1] = 0$. This results in a set of projection angles, $\Phi[m]$, $\Theta[m]$, and extents, $K_{\max}[m]$ yielding the anisotropic FOV described in (13).

D. Reconstruction

All images were reconstructed with the gridding algorithm [22], and PSFs were calculated by gridding data of all ones. Each data point is multiplied by a density compensation factor (dcf) to correct for the unequal sample spacing, which results in coloring of the noise and an intrinsic loss in the signal-to-noise ratio (SNR) efficiency [23]. The dcf can be separated into a radial and angular components, where the angular component accounts for the anisotropic projection spacing. The angular dcf is chosen so that the same radial dcf can be used on each projection, provided they all have an equal number of identically distributed radial samples. When the samples are equally spaced this radial component is linear for 2-D PR and quadratic for 3-D PR.

The 2-D angular dcf (D_θ) is proportional to the projection separation, Δk_ϕ , given from (5). For a separable dcf, D_θ must also be proportional to the projection length because the scaling of the radial sample spacing by k_{\max} cannot be described in a single radial dcf. The resulting 2-D PR angular dcf is

$$D_\theta(\Theta[n]) = K_{\max}[n] \cdot \Delta k_\phi = \frac{K_{\max}[n]}{FOV(\Theta[n] + \frac{\pi}{2})}. \quad (20)$$

For anisotropic 3-D cones, this compensation factor is applied to each cone by dividing [3, eq. (10)] by D_θ . In 3-D PR, the density compensation for a given projection is found by multiplying the compensation factors for the polar and azimuthal sampling

$$\begin{aligned} D_{3-D}(\Theta[n], \Phi[m_n]) \\ = D_\theta(\Theta[n]) \times D_\phi(\Phi[m_n]) \\ = \frac{K_{\max}[n]}{FOV_\theta(\Theta[n] + \frac{\pi}{2}) \times FOV_\phi(\Phi[m_n] + \frac{\pi}{2})}. \end{aligned} \quad (21)$$

For the full-projection spiral-based design, this dcf is slightly modified as described in Appendix I.

E. Design Functions

The anisotropic FOVs were designed in Matlab 7.0 (The Mathworks, Natick, MA). The design functions for 2-D PR, 3-D cones, and both 3-D PR methods, along with accompanying documentation are available for general use.¹

F. MRI Experiments

A GE Excite 1.5 T scanner with gradients capable of 40 mT/m amplitude and 150 T/m/s slew rate (GE Healthcare, Milwaukee, WI) was used for all experiments. The 2-D PR images were acquired with a UTE sequence using half-projection acquisitions, 5 mm slice thickness, TE = 500 μ s, TR = 100 ms, 30° flip angle, 512 samples per projection, and 1 mm resolution with a transmit/receive extremity coil. The 3-D PR images were acquired with a spoiled gradient-recalled echo (SPGR) sequence using full-projection acquisitions with TE = 3 ms and TR = 10 ms. The bottle phantom images used a 15° flip angle, 256 samples per projection, and 1 mm isotropic resolution with a transmit/receive head coil. The *in vivo* images used a 30° flip angle, 3 cm slab-selective RF excitation, 192 samples per projection, a body coil, and were acquired in a single

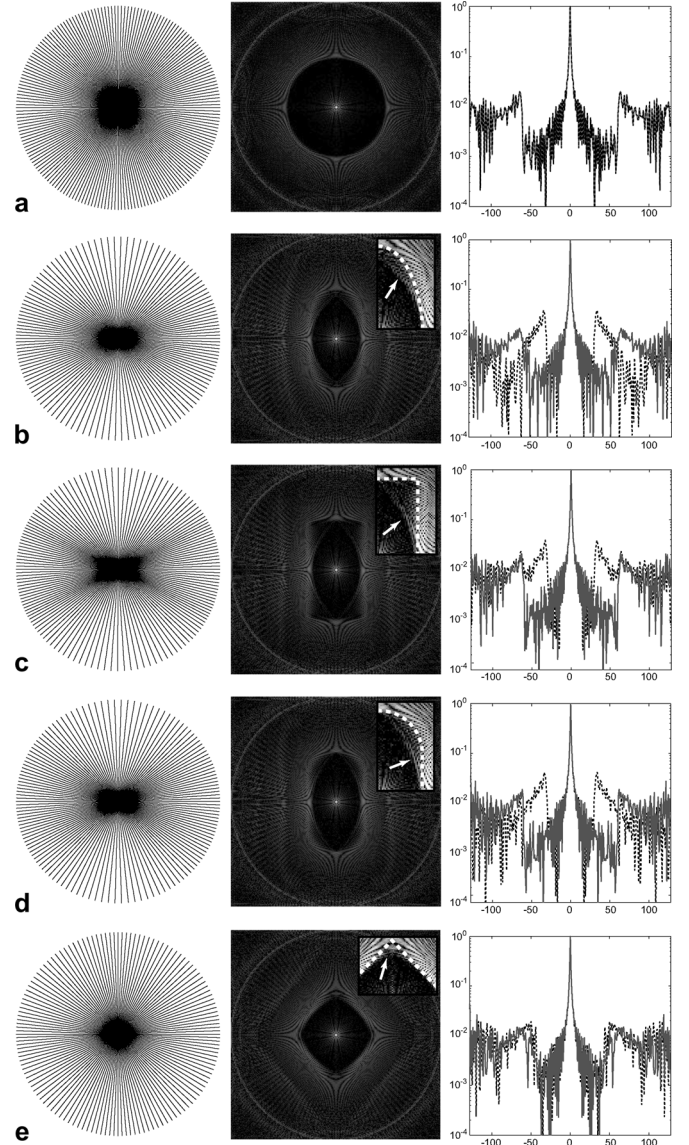


Fig. 6. Projection sampling patterns (left column) and PSFs (middle column), with plots along x (black, dashed line) and y (gray line) axes in the right column. FOV shapes: (a) circle, (b) ellipse, (c) rectangle, (d) oval, and (e) diamond. Inset PSF images are windowed narrowly to show the low-level aliasing (arrows) within the desired FOV (dashed lines). Plots show the aliasing peaks and the isotropic resolution in the central lobes. Small FOVs are used for visualization of the variable angular density.

25-s breath-hold. Both fully-sampled and undersampled cylindrical FOVs with 3 and 2 mm isotropic resolution, respectively, are compared to isotropic FOVs requiring the same number of projections.

IV. RESULTS

A. Two-Dimensional PSFs

Fig. 6 shows some sampling patterns designed with the 2-D anisotropic FOV algorithm and their corresponding PSFs, showing that the desired FOV shapes are achieved. They have isotropic resolution, as shown in the PSF central lobes. There is some low-level aliasing introduced inside the desired FOV for the anisotropic shapes, shown in the inset PSF images. See Section V for a full discussion.

¹http://www-mrsrl.stanford.edu/~peder/radial_fovs

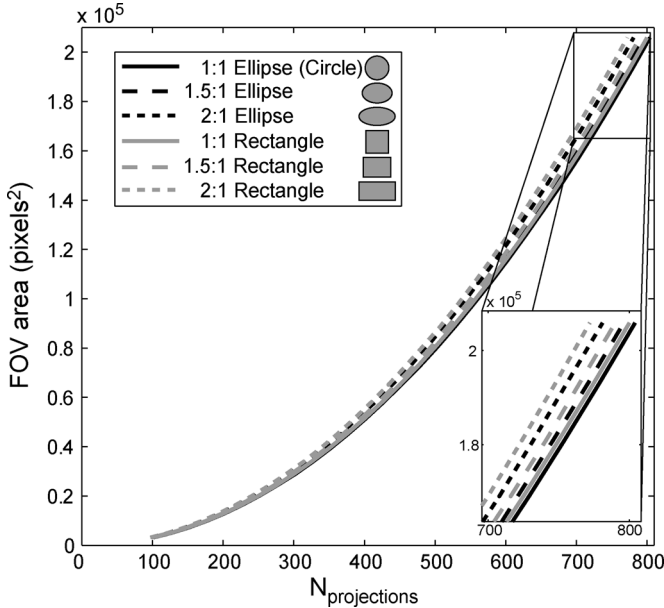


Fig. 7. Number of projections for elliptical and rectangular FOV shapes versus the resulting FOV area. All the FOVs have 1 pixel isotropic resolution. There is no loss in efficiency by using anisotropic shapes, and in fact they are slightly more efficient than the isotropic case. This increase in efficiency comes at the cost of low-level aliasing within the FOV, seen in Fig. 6.

Fig. 7 shows the relationship between the number of projections and the FOV area for elliptical and rectangular FOV shapes. The relationship is quadratic for a circular FOV, and the other shapes are also approximately quadratic. The anisotropic shapes are slightly more efficient, with efficiency increasing as the shapes become narrower. This is due to the low-level aliasing seen in Fig. 6, which is larger for narrower shapes (see Section V).

Some sampling patterns with variable k_{\max} patterns and their corresponding PSFs are shown in Fig. 8. The angularly varying projection lengths results in anisotropic resolution, seen in the main lobe of the PSFs. There is again some low-level aliasing introduced inside the desired FOV in Fig. 8(a) and (e), but there is none of this aliasing in Fig. 8(b)–(d). For these three sampling patterns, k_{\max} is the dual of the FOV shape, or $k_{\max}(\phi) \propto \text{FOV}(\phi + (\pi/2))$. In this case, the width of the aliasing lobes is inversely proportional to the FOV and the angular density compensation, D_θ , is uniform (20). See Section V for more discussion of the dual shapes. Reducing the resolution also reduces the number of projections required. For the same FOV shapes with isotropic resolution, the trajectories in Fig. 8 require between 13% and 36% less projections, demonstrating the trade-off that can be made between resolution in a given dimension and acquisition time.

Animations of how the PSF evolves as the algorithm progresses are available.² The principles of the sampling approximations used (Fig. 1) are visible in the movies.

B. Three-Dimensional PSFs

The PSFs for 3-D cones trajectories are 2-D PR PSFs rotated about one axis, as is illustrated in Fig. 4(a) and (b).

²http://www-mrsrl.stanford.edu/~peder/radial_fovs

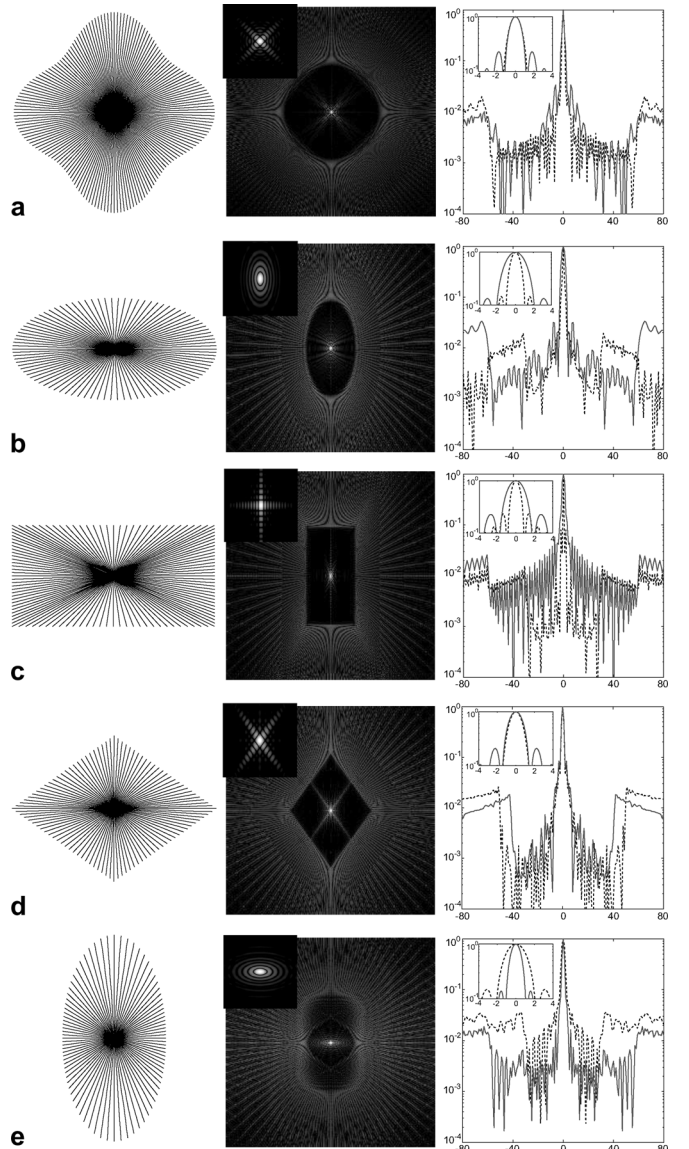


Fig. 8. Variable k_{\max} sampling patterns (left column) and PSFs (middle column, plots in right column), with enlarged views of the central lobe inset. The black, dashed line plot is along the x -axis, and the gray line is along the y -axis in (b), (c), and (e), and along $x = y$ in (a) and (d). FOV / k_{\max} shapes: (a) circle/star, (b) ellipse/ellipse, (c) rectangle/rectangle, (d) diamond/diamond, and (e) oval/ellipse. All the combinations have a minimum resolution size of 1 pixel, with maximum resolutions two pixels in (a), (b), and (e), 1.72 pixels in (c), and 1.33 pixels in (d). Shape combinations in (b), (c), and (d) have no low-level aliasing inside the FOV shape, unlike (a) and (e), and the isotropic resolution projections in Fig. 6. Small FOVs are used for visibility of the variable angular density.

Fig. 9 shows some PSFs for spiral-based 3-D PR sampling patterns. For the variety of shapes and dimensions, the desired FOV is achieved, and using an oval for FOV_θ and ellipse for FOV_ϕ [Fig. 9(a)] results in three different FOV dimensions. There are low-level aliasing artifacts present in these PSFs [arrows in Fig. 9(a) and (b)]. The cuboid [Fig. 9(c)] has sharp corners in all three dimensions, and is also well-defined at nonzero z values, demonstrating that the azimuthal sampling aliasing shape, FOV_ϕ , is invariant in z , as assumed in (13). The PSF of an ellipsoid FOV with an ellipsoid $k_{\max,\theta}$ is shown in Fig. 9(d), demonstrating that variable $k_{\max,\theta}$ is feasible. This trajectory

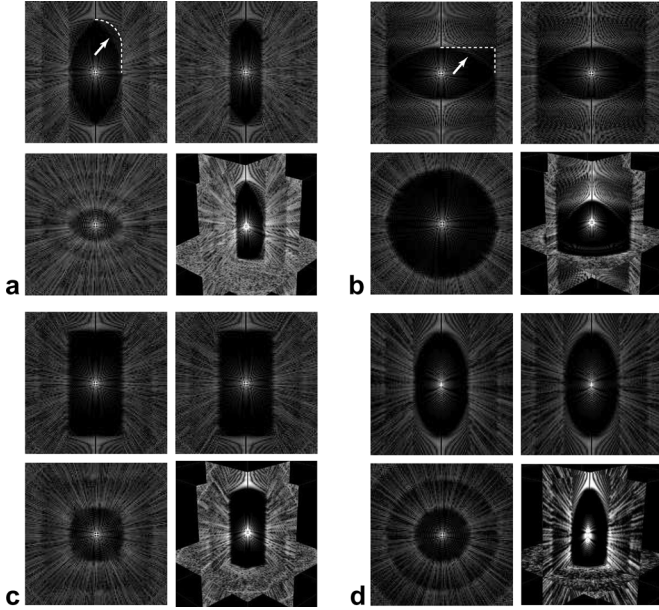


Fig. 9. PSFs for 3-D PR trajectories with anisotropic FOVs using the spiral-based design. FOVs: (a) oval FOV_θ and ellipse FOV_ϕ , (b) cylinder, (c) cuboid, and (d) ellipsoid with an ellipsoid $k_{\max,\theta}$ shape, shrunk in the k_z direction. Top row for each shape shows the PSF in the $y = 0$ and $x = 0$ planes, and the bottom row shows the $z = 0$ plane and a three-plane view. Similarly to the 2-D case, there is some low-level aliasing (arrows) inside the desired FOV shapes (dashed lines), which is particularly visible in (b).

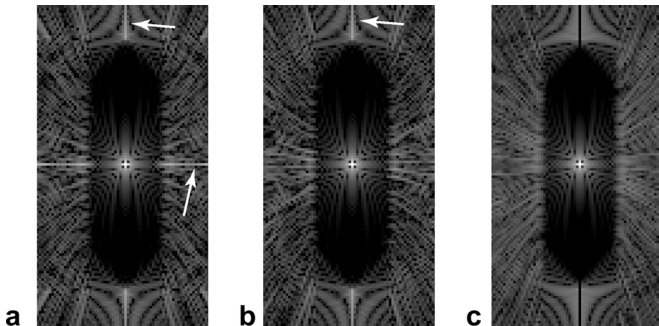


Fig. 10. PSFs for various 3-D PR design methods. (a) Cones-based design without randomized ϕ_0 . (b) Cones-based design with randomized ϕ_0 . (c) Spiral-based design. The $x = 0$ plane for the shape in Fig. 9(a) is shown, and the images are identically windowed. The arrows indicate coherent streaking artifacts, all of which are eliminated when using the spiral-based design.

has a 50% reduction in Z gradient strength requirements compared to the other trajectories because $k_{\max,\theta}$ limits the projection extents in k_z . This halves the resolution in z , but requires 33% less projections than the same FOV shape with 1 pixel isotropic resolution.

Coherent aliasing lines are introduced when using the cones-based design, as shown in Fig. 10. The use of a random ϕ_0 in the cones-based design eliminates the coherent line in the $x - y$ plane. A line along the z axis remains because the polar projection spacings around $\theta = \pi/2$ are all identical. The tilt of the spiral in k_z diffuses the line in the spiral-based design. These coherent lines would not affect fully-sampled acquisitions. In undersampled applications, which take advantage of the diffuse 3-D PR aliasing, this could cause artifacts, making the spiral-based design advantageous.

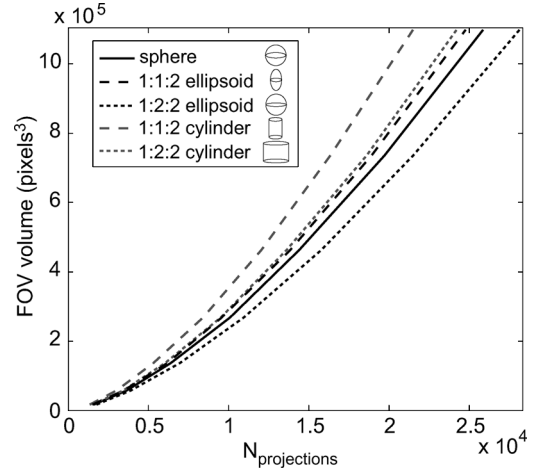


Fig. 11. Number of projections for 3-D anisotropic FOV shapes, with ratios of $x : y : z$ lengths, versus the shape volume. All FOVs have 1 pixel isotropic resolution, and the curves shown are for both the cones-based and spiral-based design methods. Most of the anisotropic shapes are actually more efficient than the sphere, but at the cost of low-level aliasing within the FOV, seen in Fig. 9.

The scan volume efficiency for some 3-D anisotropic FOV shapes is shown in Fig. 11. The anisotropic shapes are generally more efficient, although there is more variation in efficiency than in the 2-D case (Fig. 7). The increased efficiency is at the expense of some low-level aliasing inside the FOV. The 1:1:2 ($x : y : z$) shapes only have anisotropy in the polar sampling, and they are more efficient than the 1:2:2 shapes that also have azimuthal sampling anisotropy. This difference is caused by the anisotropic FOV_ϕ cutting off portions of FOV_θ , which can be seen in Fig. 4.

C. MRI Experiments

In vivo 2-D PR leg images acquired with isotropic and anisotropic FOVs are shown in Fig. 12. The reduced FOV images [Fig. 12(b)–(d)] were acquired with half the number of projections as the full FOV image [Fig. 12(a)]. The isotropic reduced FOV [Fig. 12(d)] results in significant streaking aliasing artifacts, while using anisotropic reduced FOVs tailored to the shape of the leg [Fig. 12(b) and (c)] results in no increase in artifact compared to the full isotropic FOV image. The images without aliasing [Fig. 12(a)–(c)] are all slightly undersampled, as shown by the overlaid FOV shapes, but no aliasing is visible due to the relatively diffuse aliasing pattern of PR.

Fig. 13 shows a representative slice from 3-D PR acquisitions of a water bottle phantom using different FOVs, each with the same number of projections. In the isotropic FOV acquisitions, streaking artifacts are visible within the bottle and emanate from the edge of the bottle [arrows in Fig. 13(a) and (b)] because the FOV is not large enough. These artifacts have a peak amplitude of 23.2% of the signal for the cones-based design and 11.5% for the spiral-based design. By using a fully-sampled cylindrical FOV that matches the bottle's shape, these streaks are completely shifted outside of the bottle [arrows in Fig. 13(c) and (d)]. The differences in aliasing diffusivity between the two 3-D PR design methods, shown in the PSFs in Fig. 10, can also be seen in the images. There is a single, prominent aliasing streak when

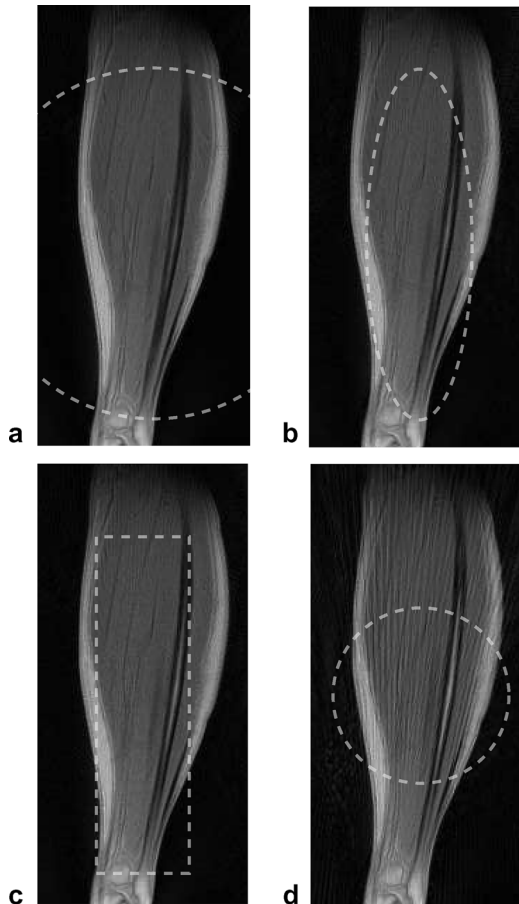


Fig. 12. Two-dimensional PR lower leg images with various FOV shapes, shown by the dashed lines. (a) 25-cm circular FOV requiring 393 projections, (b) 7.5×25 -cm elliptical FOV requiring 197 projections, (c) 6.5×24 cm rectangular FOV requiring 195 projections, (d) 12.5-cm circular FOV requiring 196 projections. Noncircular FOV images (b), (c) show no increase in aliasing artifacts or loss of resolution but were acquired with half the projections. Circular FOV acquired with half the projections (d) results in significant aliasing artifacts.

using the cones-based design (long, thin arrows), which is diffused with the spiral-based design (short, fat arrows), and the peak aliasing amplitudes also reflect this difference.

In vivo 3-D PR images of a 3-cm abdomen slab acquired in a single breath-hold are shown in Figs. 14 and 15. The isotropic FOV images have significant streaking artifacts within the abdomen [arrows in Fig. 14(a) and Fig. 15(a)] because of the high undersampling ratios. Using a thin, squished cylindrical FOV tailored to the anatomy and the excited slab eliminates these streaking artifacts, as shown in Fig. 14(b). A small degree of undersampling in this tailored FOV is also tolerated, as evidenced by the lack of streaking artifacts in Fig. 15(b). The isotropic FOV streaking also results in a higher level of signal outside of the body in the axial images. More streaking is seen just outside the slab in the coronal images with the anisotropic FOV [arrows in Fig. 14(b)]. This is expected because of the smaller superior-inferior dimension with the anisotropic FOV relative to the spherical FOV, for which the streaks in this dimension are outside of the displayed region. Acquiring the equivalent fully-sampled 36 cm isotropic FOV at 3 mm isotropic resolution requires 22 656 projections, while an equivalent undersampled 19.6 cm

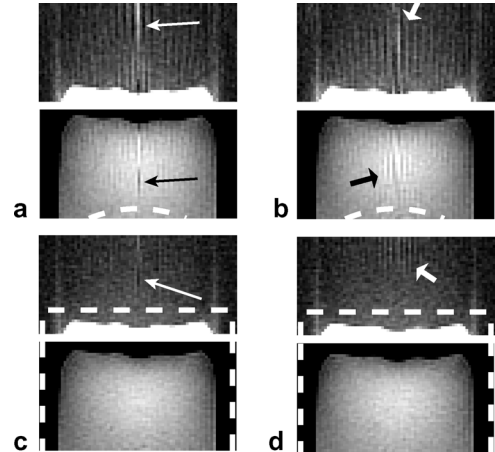


Fig. 13. Three-dimensional PR phantom images, all acquired with the same number of projections. Isotropic FOV using the (a) cones-based method and (b) spiral-based method. Cylindrical FOV using the (c) cones-based method and (d) spiral-based method. Top images are all windowed identically to show the aliasing artifacts outside the bottle (white arrows). Bottom images are also identically windowed to show the aliasing artifacts within the bottle for the undersampled, isotropic FOVs (black arrows). Dashed lines indicate the supported FOV.

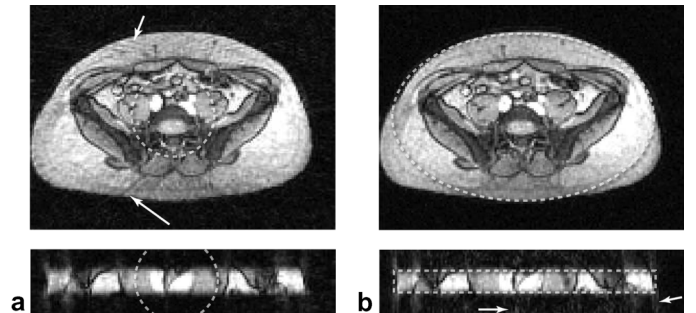


Fig. 14. Axial (top) and coronal (bottom) slices from a thin-slab 3-D PR abdomen data-set with 3-mm isotropic resolution acquired in a single breath-hold. (a) Isotropic 11.4 cm FOV requiring 2303 projections. (b) Cylindrical $36 \times 23 \times 3$ cm FOV requiring 2368 projections. Both trajectories were designed using the spiral-based method. Streaking artifacts result from the high axial undersampling of the isotropic FOV [arrows in (a)]. Tailoring FOV eliminates these artifacts by reducing FOV in the slab dimension. This leads to the streaks in the coronal slice [arrows in (b)], but these are outside of the imaging volume.

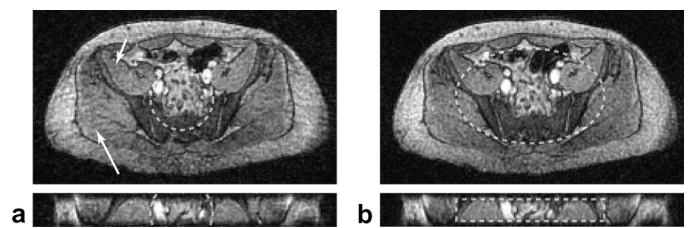


Fig. 15. Same as Fig. 14, except with 2 mm isotropic resolution and increased undersampling. (a) Isotropic 8-cm FOV requiring 2519 projections. (b) Cylindrical $19.6 \times 12.2 \times 2.8$ cm FOV requiring 2529 projections. The undersampled cylindrical FOV has no noticeable streaking artifacts, which obscure the anatomy with the isotropic FOV (arrows).

FOV at 2 mm resolution requires 14 744 projections, both of which are prohibitively large for single breath-hold imaging.

V. DISCUSSION

The algorithms presented are designed with fully-sampled FOV parameters, but will also be beneficial for undersampled radial imaging applications, as demonstrated in Fig. 15. For undersampled applications like VIPR [7], the desired FOV shape and size should be a scaled down version of the region-of-interest for equivalent undersampling factors in every dimension. The anisotropic FOV projections can also be applied to the highly constrained backprojection (HYPR) method for time-resolved MRI [24] because they can be reconstructed by filtered backprojection. Exam-specific FOVs can be used in all applications because the computation time of the design algorithms is small. Using an initial localizing scan, the desired FOV could be drawn or automatically detected and the acquisition tailored appropriately.

For some FOV and k_{\max} shapes, the resulting PSFs have low-level aliasing within the desired FOV. This is due to the finite width of the aliasing lobes, as shown in Fig. 1(b), which is not accounted for in our design algorithms. The projection angles are designed based on the peak at the center of these aliasing lobes, leaving the potential for up to half of the lobe to overlap inside the FOV. Overlap is more likely to occur as the radial separation of neighboring lobes increases, and thus is correlated with $|d\text{FOV}(\phi)/d\phi|$. The online animations of the PSFs show how the origin of the low-level aliasing is primarily along the longer edges where this derivative is the largest. No aliasing originates from minima or maxima of the FOV where the angular derivative is zero.

Narrower shapes, which have a larger angular derivative, have more desirable efficiency curves in Fig. 7 because they have more low-level aliasing within the FOV. For the shapes in Fig. 7, the total low-level aliasing power is approximately 0.60% and 1.3% of the main lobe power for the 1.5:1 and 2:1 ellipses, respectively, and 0.67%, 0.91%, and 1.2% for the 1:1, 1.5:1, and 2:1 rectangles. This confirms that narrower shapes have more low-level aliasing and that, in general, this aliasing is small.

There is no low-level aliasing in the dual shape sampling patterns seen in Fig. 8(b)–(d). This suggests that the low-level aliasing may be more correctly correlated with the derivative of $\text{FOV}(\phi)/k_{\max}(\phi + (\pi/2))$, which is zero for the dual shapes. This derivative is very large for the FOV and k_{\max} shapes in Fig. 8(e), which has significant aliasing inside the desired FOV. Another observation is that dual ellipse sampling can be formed by scaling an isotropic sampling pattern along one axis. By Fourier theory, this transformation scales the PSF along the corresponding axis by the inverse and introduces no low-level aliasing. It is possible that the other shapes may be formed by some transformation of isotropic case. We have found no derivation confirming this suggested low-level aliasing correlation or any general transformation starting with isotropic sampling.

With our method, it is possible to use 3-D radial imaging trajectories to image thin slabs with isotropic resolution, as demonstrated in Figs. 14 and 15. Previously, this was achieved by using stacks of projections [6], [9], which lacks some of the benefits of a true 3-D radial acquisition, such as ultra-short TEs. Stacking the projections also results in a coherent aliasing streak along the stacking direction, similar to the streak resulting from the

cones-based design (see Fig. 10), which may be related to artifacts reported in the stacking dimension with contrast enhancement [7]. Both methods support one dimension of variable resolution, and stacks of 2-D anisotropic FOV projections are also possible.

This projection design can also be applied to other centric-based k -space trajectories. It can be directly applied to twisting radial-line (TwRL) trajectories [25] by specifying the angular spacing of the different acquisitions. Anisotropic resolution can also be incorporated by adjusting the twist in the radial line to match $k_{\max}(\phi)$. Interleaved spiral acquisitions can also be adjusted for anisotropic FOVs. The angular spacing of adjacent interleaves can be determined by our algorithm, and spirals with many interleaves will benefit the most from this adjustment. This could also be combined with the previous anisotropic FOV spiral method [26] which describes the design of the spirals themselves.

VI. CONCLUSION

We have introduced a new method that designs projections for anisotropic FOVs in radial imaging. These FOVs can be precisely tailored to noncircular objects or regions-of-interest in 2-D and 3-D imaging. This allows for scan time reductions without introducing aliasing artifacts. For undersampled applications, this method allows for reduction of aliasing artifacts.

Algorithms have been presented for the design of 2-D and 3-D PR trajectories, as well as 3-D cones. There is no loss in FOV area efficiency when using anisotropic FOVs. The algorithms are very simple and fast, allowing them to be computed on-the-fly. They also support variable trajectory extents which can be used in MRI to favor certain gradients or relax gradient constraints in 3-D cones.

APPENDIX I FULL-PROJECTION SPIRAL-BASED DESIGN

For a spiral-based full-projection design, the spiralling path is sampled for $0 \leq \theta \leq (\pi/2)$ by using $\theta_{\text{width}} = \pi/2$ for the set of initial polar samples, and interpolating to $\hat{\Theta}[N_{\text{polar}} + 1] = \pi/2$ and $\hat{K}_{\max}[N_{\text{polar}} + 1] = k_{\max,\theta}(\pi/2)$. Near $\theta = \pi/2$, the polar sample spacing is not as desired because the opposite ends of the full-projections are spiralling in opposing directions. The spacing between these opposing turns varies approximately linearly from 1.5 to 0.5 times the desired spacing over each of the final two half-turns of the spiral. This spacing discrepancy also occurs with the isotropic 3-D PR spiral design for full-projections [21]. This undersampling can be compensated for by adding an extra quarter-turn to the spiral. To do this, the interpolation is carried out to additional samples of $\hat{\Theta}[N_{\text{polar}} + 2] = (\pi/2) + (4k_{\max,\phi}\text{FOV}_\theta(\pi))^{-1}$ and $\hat{K}_{\max}[N_{\text{polar}} + 2] = k_{\max,\theta}(\hat{\Theta}[N_{\text{polar}} + 2])$, with $N_{N_{\text{polar}}+1,\text{est}} = N_{\phi,\text{est}}/4$.

The density compensation must also be slightly modified to accommodate both the opposing spiral paths and the extra quarter-turn. Based on the 3-D spiral geometry, it can be found that the total spacing from adjacent turns decreases approximately linearly between 1 and 0.5 times the desired spacing identically over the two last half-turns. Thus, the dcf from (21) is weighted over each of the half-turns separately by a linear ramp from 1 to 0.5 as θ increases.

REFERENCES

- [1] P. C. Lauterbur, "Image formation by induced local interactions: Examples employing nuclear magnetic resonance," *Nature*, vol. 242, pp. 190–191, May 1973.
- [2] P. Irarrazabal and D. G. Nishimura, "Fast three dimensional magnetic resonance imaging," *Magn. Reson. Med.*, vol. 33, no. 5, p. 656, May 1995.
- [3] P. T. Gurney, B. A. Hargreaves, and D. G. Nishimura, "Design and analysis of a practical 3-D cones trajectory," *Magn. Reson. Med.*, vol. 55, no. 3, pp. 575–582, Mar. 2006.
- [4] G. H. Glover and J. M. Pauly, "Motion artifact reduction with projection reconstruction imaging," *Magn. Reson. Med.*, vol. 28, no. 2, pp. 275–289, Dec. 1992.
- [5] D. Nishimura, J. I. Jackson, and J. M. Pauly, "On the nature and reduction of the displacement artifact in flow images," *Magn. Reson. Med.*, vol. 22, no. 2, pp. 481–492, Dec. 1991.
- [6] D. C. Peters, F. R. Korosec, T. M. Grist, W. F. Block, J. E. Holden, K. K. Vigen, and C. A. Mistretta, "Undersampled projection reconstruction applied to MR angiography," *Magn. Reson. Med.*, vol. 43, no. 1, pp. 91–101, Jan. 2000.
- [7] A. V. Barger, W. F. Block, Y. Toropov, T. M. Grist, and C. A. Mistretta, "Time-resolved contrast-enhanced imaging with isotropic resolution and broad coverage using an undersampled 3-D projection trajectory," *Magn. Reson. Med.*, vol. 48, no. 2, pp. 297–305, Aug. 2002.
- [8] A. Lu, E. Brodsky, T. M. Grist, and W. F. Block, "Rapid fat-suppressed isotropic steady-state free precession imaging using true 3-D multiple-half-echo projection reconstruction," *Magn. Reson. Med.*, vol. 53, no. 3, pp. 692–699, Mar. 2005.
- [9] K. K. Vigen, D. C. Peters, T. M. Grist, W. F. Block, and C. A. Mistretta, "Undersampled projection-reconstruction imaging for time-resolved contrast-enhanced imaging," *Magn. Reson. Med.*, vol. 43, no. 2, pp. 170–176, Feb. 2000.
- [10] C. Stehning, P. Börnert, K. Nehrke, H. Eggers, and O. Dössel, "Fast isotropic volumetric coronary MR angiography using free-breathing 3-D radial balanced FFE acquisition," *Magn. Reson. Med.*, vol. 52, no. 1, pp. 197–203, Jul. 2004.
- [11] C. Stehning, P. Börnert, K. Nehrke, H. Eggers, and O. Dössel, "Free-breathing whole-heart coronary MRA with 3-D radial SSFP and self-navigated image reconstruction," *Magn. Reson. Med.*, vol. 54, no. 2, pp. 476–480, Aug. 2005.
- [12] P. D. Gatehouse and G. M. Bydder, "Magnetic resonance imaging of short T2 components in tissue," *Clin. Radiol.*, vol. 58, no. 1, pp. 1–19, Jan. 2003.
- [13] M. D. Robson, P. D. Gatehouse, M. Bydder, and G. M. Bydder, "Magnetic resonance: An introduction to ultrashort TE (UTE) imaging," *J. Comput. Assist. Tomogr.*, vol. 27, no. 6, pp. 825–846, Nov./Dec. 2003.
- [14] J. Rahmer, P. Börnert, J. Groen, and C. Bos, "Three-dimensional radial ultrashort echo-time imaging with T2 adapted sampling," *Magn. Reson. Med.*, vol. 55, no. 5, pp. 1075–1082, May 2006.
- [15] P. E. Z. Larson, P. T. Gurney, K. Nayak, G. E. Gold, J. M. Pauly, and D. G. Nishimura, "Designing long-T2 suppression pulses for ultrashort echo time imaging," *Magn. Reson. Med.*, vol. 56, no. 1, pp. 94–103, Jul. 2006.
- [16] T. Gu, F. R. Korosec, W. F. Block, S. B. Fain, Q. Turk, D. Lum, Y. Zhou, T. M. Grist, V. Haughton, and C. A. Mistretta, "PC VIPR: A high-speed 3-D phase-contrast method for flow quantification and high-resolution angiography," *Am. J. Neuroradiol.*, vol. 26, no. 4, pp. 743–749, Apr. 2005.
- [17] K. Scheffler, "Tomographic imaging with nonuniform angular sampling," *J. Comput. Assist. Tomogr.*, vol. 23, no. 1, pp. 162–166, Jan./Feb. 1999.
- [18] K. Scheffler and J. Hennig, "Reduced circular field-of-view imaging," *Magn. Reson. Med.*, vol. 40, no. 3, pp. 474–480, Sep. 1998.
- [19] M. L. Lauzon and B. K. Rutt, "Effects of polar sampling in k-space," *Magn. Reson. Med.*, vol. 36, no. 6, pp. 940–949, Dec. 1996.
- [20] G. H. Glover, J. M. Pauly, and K. M. Bradshaw, "Imaging ^{11}B with a 3-D projection reconstruction method," *J. Magn. Reson. Imag.*, vol. 2, no. 1, pp. 47–52, Jan./Feb. 1992.
- [21] S. T. S. Wong and M. S. Roos, "A strategy for sampling on a sphere applied to 3-D selective RF pulse design," *Magn. Reson. Med.*, vol. 32, no. 6, pp. 778–784, Dec. 1994.
- [22] P. J. Beatty, D. G. Nishimura, and J. M. Pauly, "Rapid gridding reconstruction with a minimal oversampling ratio," *IEEE Trans. Med. Imag.*, vol. 24, no. 6, pp. 799–808, Jun. 2005.
- [23] C.-M. Tsai and D. Nishimura, "Reduced aliasing artifacts using variable-density k-space sampling trajectories," *Magn. Reson. Med.*, vol. 43, no. 3, pp. 452–458, Mar. 2000.
- [24] C. A. Mistretta, O. Wieben, J. Velikina, W. Block, J. Perry, Y. Wu, K. Johnson, and Y. Wu, "Highly constrained backprojection for time-resolved MRI," *Magn. Reson. Med.*, vol. 55, no. 1, pp. 30–40, Jan. 2006.
- [25] J. I. Jackson, D. G. Nishimura, and A. Macovski, "Twisting radial lines with application to robust magnetic resonance imaging of irregular flow," *Magn. Reson. Med.*, vol. 25, no. 1, pp. 128–139, May 1992.
- [26] K. F. King, "Spiral scanning with anisotropic field of view," *Magn. Reson. Med.*, vol. 39, no. 3, pp. 448–456, Mar. 1998.